Ion-irradiation-induced amorphization of Cu nanoparticles embedded in SiO_2

B. Johannessen,* P. Kluth, and D. J. Llewellyn
Department of Electronic Materials Engineering, Research School of Physical Sciences and Engineering, The Australian National University, Canberra ACT 0200, Australia

G. J. Foran
Australian Nuclear Science and Technology Organization, Menai NSW 2234, Australia

D. J. Cookson
Australian Synchrotron Research Program, Bldg 434, 9700 South Cass Avenue, Argonne, Illinois 60439, USA

M. C. Ridgway
Department of Electronic Materials Engineering, Research School of Physical Sciences and Engineering, The Australian National University, Canberra ACT 0200, Australia

(Received 18 February 2007; revised manuscript received 15 July 2007; published 13 November 2007)

Elemental Cu nanoparticles embedded in SiO_2 were irradiated with 5 MeV Sn^{3+}. The nanoparticle structure was studied as a function of Sn^{3+} fluence by extended x-ray absorption fine structure spectroscopy, small-angle x-ray scattering, and transmission electron microscopy. Prior to irradiation, Cu nanoparticles exhibited the face-centered-cubic structure. Upon irradiation at intermediate fluences (1×10^{13} to 1×10^{14} ions/cm^2), the first nearest neighbor Cu-Cu coordination number decreased, while the Debye-Waller factor, bondlength, and third cumulant of the bondlength distribution increased. In particular, at a fluence of 1×10^{14} ions/cm^2 we argue for the presence of an amorphous Cu phase, for which we deduce the structural parameters. Low temperature annealing (insufficient for nanoparticle growth) of the amorphous Cu returned the nanoparticles to the initial preirradiation structure. At significantly higher irradiation fluences (1×10^{15} to 1×10^{16} ions/cm^2), the nanoparticles were dissolved in the matrix with a Cu coordination similar to that of Cu_2O.

DOI: 10.1103/PhysRevB.76.184203 PACS number(s): 61.10.Ht, 81.07.Bc, 61.10.Eq

I. INTRODUCTION

Amorphous metals (metallic glasses) are an intriguing aspect of condensed matter physics, as indicated by the number of publications in the field since the report by Klement *et al.* more than four decades ago.[1] Although these materials have found application in a range of diverse fields due to their advantageous characteristics, including electronic, magnetic, and corrosion-resistant properties,[2–4] there is still discussion as to an appropriate atomic structural model. A common model involves the dense random packing of nonoverlapping ("hard") spheres,[5] in which the *maximum* number of equally sized spheres in contact with another sphere is 12,[6] i.e., equal to the first nearest neighbor coordination number found in face-centered-cubic (fcc) structures. The coordination number is related to the packing density, η, which is 0.74 for the fcc structure.[7] The hard spheres model predicts $\eta\sim0.64$ for amorphous metals (with equal sized spheres),[5] which corresponds to a first nearest neighbor coordination number of $\sim$7.[7] Experimentally, however, amorphous metals are only 0.5–2.0 % less dense ($\eta\sim0.72$–0.74) than the corresponding crystalline structure,[5] which corresponds to a coordination number of $\sim$10. Consequently, refined packing models in which the atoms fill space more efficiently have been proposed.[8]

Amorphous metals are commonly alloys comprised of at least two different atomic species in order to stabilize the amorphous structure. Pure elemental amorphous metals, which are disordered locally, but not chemically, can easily crystallize at low temperatures. Hence the production of elemental amorphous metals require an extremely rapid cooling rate (of the order of 10^9 K/s or faster[9]) from the melt. This is possible with a sonochemical process as demonstrated for amorphous Fe,[9] Ni,[10] and Cu.[11] The latter two reports do not provide information on the short-range atomic structure, whereas the former reports a first shell coordination number of 10, consistent with a packing density $\eta\sim0.73$.[7]

Ion irradiation of bulk elemental metallic substrates induces displaced and recoiled atoms which can yield a collision cascade with a molten core, the latter apparent in molecular dynamics simulations.[12] However, the molten core rapidly recrystallizes and only small defect clusters remain. Upon further ion irradiation, the extent of disorder saturates and the substrate retains crystallinity.[12,13] We recently reported the ion-irradiation-induced amorphization of elemental *semiconductor* (Ge) nanoparticles embedded in amorphous SiO_2 using 5 MeV Si^{2+}.[14] The nanoparticles were rendered amorphous at fluence approximately two orders of magnitude below that required for the corresponding bulk material. Several contributing factors were suggested, including the pre-irradiation, higher-energy structural state of the nanoparticles and preferential nucleation of the amorphous phase at the nanoparticle/SiO_2 interface.[14] Furthermore, MeV ion irradiation of thin amorphous SiO_2 films leads to compaction and stress.[15,16] This could also influence the structural parameters for the nanoparticles embedded within the film and potentially lower the energy barrier for amorphization. We now thus investigate ion irradiation of

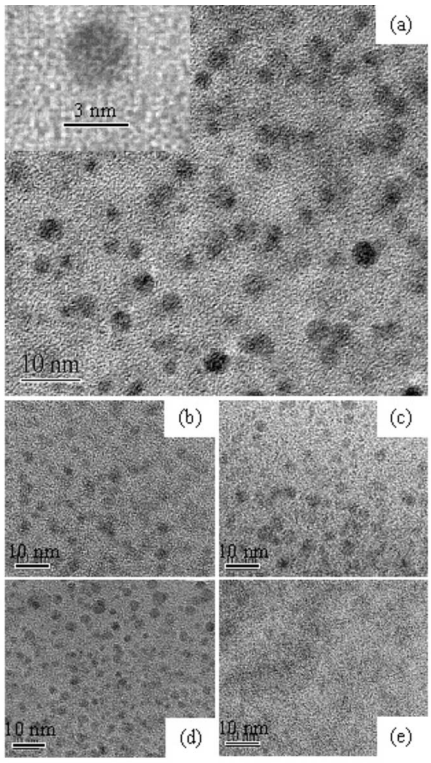

FIG. 1. XTEM micrographs of Cu nanoparticle samples: (a) Unirradiated, and after ion irradiation to a fluence of (b) 6×10^{13}, (c) 1×10^{14}, (d) 3×10^{14}, and (e) 1×10^{15}/cm^2. Inset in (a) is a high-resolution image of an individual nanoparticle where the (111) lattice planes of fcc Cu are discernible.

embedded elemental *metal* (Cu) nanoparticles as a potential route to the amorphous phase.

Both crystalline and amorphous matrices can influence the nanoparticle properties. For example, superheating has been reported for nanoparticles embedded in both crystalline (Tl in Al,[17] Ar in Al[18]) and amorphous hosts (Ge in SiO_2[19]). In the latter paper, it was suggested that interfacial energies (between the matrix and the liquid/solid nanoparticles), as opposed to epitaxy, are influencing the melting point characteristics of embedded nanoparticles. Recently, nonlinear optical properties of Cu nanoparticles embedded in crystalline and amorphous SiO_2 were investigated.[20] The third order susceptibility, indicative of nanoparticle formation, was dependent on the implantation flux, but not on the nature of the matrix. Though the report did not investigate the nanoparticle morphology, Cu implanted into crystalline $LiNbO_3$ has been reported to produce nonspherical nanoparticles.[21] However, the level of radiation-resistance to amorphization of the host matrix may be an issue as reported for Cu implanted into crystalline GaAs.[22]

The present article is a comprehensive study of 5 MeV Sn^{3+} ion-irradiation-induced structural changes in Cu nanoparticles embedded in an amorphous SiO_2 matrix and follows our recent preliminary publication.[23] We seek to identify and understand the short-range atomic structure of the amorphous Cu phase for both fundamental insight and potential technological applications. We utilize transmission

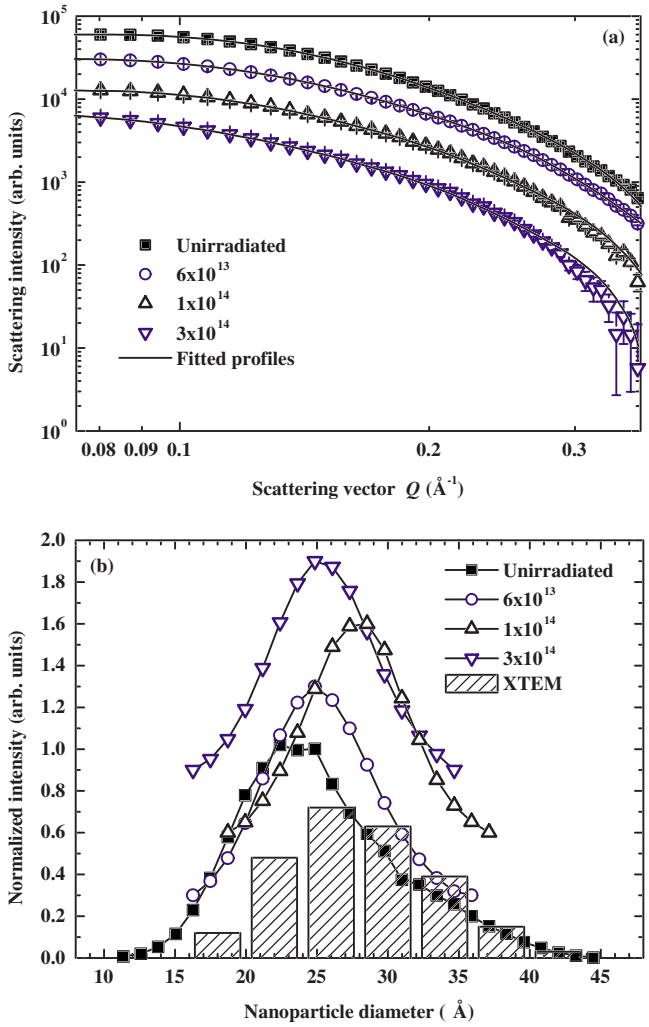

FIG. 2. (Color online) SAXS analysis and results: (a) SAXS profile and fitted data for the unirradiated nanoparticles and as a function of ion irradiation fluence (offset) and (b) the volume-weighted size distributions as a function of ion irradiation fluence (offset) including the size distribution determined by XTEM for comparison (unirradiated sample only).

electron microscopy (TEM) together with a combination of synchrotron radiation based techniques to characterize our ion irradiated Cu nanoparticles. Extended x-ray absorption fine structure (EXAFS) spectroscopy has previously proven to be well suited for the determination of the short-range atomic order in Cu nanoparticles,[24] while small-angle x-ray scattering (SAXS) provides information about the nanoparticle size distribution and average diameter as a function of ion irradiation fluence.

II. EXPERIMENT

Cu^+ ions were implanted into 2 μm thick amorphous SiO_2 films, the latter grown by wet thermal oxidation of Si (100) substrates. A multiple energy (0.7, 0.9, 1.2, 1.5 MeV), multiple fluence (2.1, 4.2, 5.2, 7.2×10^{16} ions/cm^2) implant sequence yielded a near-constant Cu concentration of

TABLE I. SAXS analysis: Volume-weighted average nanoparticle diameter as a function of ion irradiation fluence.

Fluence (Sn^{3+} ions/cm^2)	Nanoparticle diameter (Å)
0	25
1×10^{13}	25
3×10^{13}	25
6×10^{13}	24
1×10^{14}	27
2×10^{14}	28
3×10^{14}	25

~3.6 at. % over a depth range of ~0.6–1.0 μm, as estimated using transport of ions in matter (TRIM) Monte Carlo simulations.[25] To minimize diffusion, implantations were performed at liquid N_2 temperature (LNT) and fluxes were maintained at power levels <0.7 W/cm^2. Following implantation, the supersaturated samples were annealed in flowing forming gas (5% H_2+95% N_2) for one hour at a temperature of 650 °C to induce precipitation and nanoparticle growth. A bulk Cu standard was prepared by depositing 220 nm of Cu on SiO_2 by thermal evaporation. The Cu layer was polycrystalline and approximately ten times the effective thickness of the implanted Cu^+ ions. To achieve a comparable thickness of SiO_2 overlayer for both the nanoparticle and polycrystalline samples, 0.6 μm of SiO_2 was then deposited on top of the Cu layer by plasma enhanced chemical vapor deposition.

The Cu nanoparticles and bulk Cu standard were irradiated simultaneously with 5.0 MeV Sn^{3+} ions in the fluence range 10^{13}–10^{16} ions/cm^2 at LNT. The ion energy was chosen to yield a projected range beyond the SiO_2 film (i.e., within the Si substrate) to negate impurity effects due to Sn. The ion energy loss due to nuclear and electronic stopping at ~0.6 μm was, respectively, 0.8 and 1.4 keV/nm in SiO_2 and 2.4 and 2.3 keV/nm in Cu as simulated by TRIM.[25]

The Cu distribution in the SiO_2 samples was probed by Rutherford backscattering spectroscopy (RBS). The depth distribution of implanted Cu was consistent with TRIM simulations (not shown) and remained virtually unchanged upon annealing or irradiation. Cross-sectional TEM (XTEM) samples were prepared using standard techniques at low temperatures to inhibit diffusion and/or recrystallization during preparation. For example, glue curable at room temperature under UV light was utilized and Ar ion milling was performed at LNT. XTEM analysis was carried out at 300 keV and exposure to the electron beam was minimized. The nanoparticle shape, size and crystallinity were investigated.

The nanoparticle size distribution was also determined with transmission SAXS measurements using 1.5 Å wavelength x rays (8.27 keV) at beamline 15ID-D of the Advanced Photon Source, USA. The volume-weighted size distribution and volume-weighted average diameters were calculated. To eliminate parasitic scattering, the substrate was removed prior to exposure (as described below). The scattered intensity profile $I(Q)$ was recorded 555 mm behind the sample with a CCD detector as a function of the scattering vector Q [where Q is $(4\pi/\lambda)\sin\theta$, λ is the wavelength of the incident x rays and θ is half the scattering angle.[26]] The samples were sufficiently thin to avoid multiple scattering effects and the parasitic scattering from air was subtracted from the total experimental scattering function. Quantitative analysis over a Q range of ~0.075–0.35 Å^{-1} was based on an indirect transform method,[27] where the most likely size distribution is recovered without an initial assumed model distribution.[28]

The short-range atomic structure of the nanoparticle samples and bulk standards was probed by EXAFS spectros-

TABLE II. Cu-Cu EXAFS analysis: Structural parameters of bulk Cu and Cu nanoparticle samples as a function of ion irradiation fluence extracted by first nearest Cu neighbor EXAFS analysis (k^3 weighted). For bulk Cu, a third cumulant was not measurable.

Sample	Coordination number (atoms)	Bondlength (Å)	Debye-Waller factor ($\times10^{-3}$ Å^2)	Third cumulant ($\times10^{-5}$ Å^3)
Unirr. standard	12 (fixed)	2.539±0.001	2.3±0.1	
1×10^{13}	12.3±0.7	2.540±0.003	2.5±0.5	
3×10^{13}	12.0±0.9	2.542±0.002	2.5±0.4	
6×10^{13}	12.4±0.8	2.538±0.003	2.5±0.3	
1×10^{14}	12.3±0.6	2.541±0.005	2.4±0.6	
2×10^{14}	11.9±0.9	2.539±0.003	2.4±0.7	
3×10^{14}	12.2±1.1	2.538±0.006	2.3±0.4	
Unirr. nanoparticles	10.1±1.1	2.520±0.006	4.9±0.7	0.6±8.0
1×10^{13}	8.5±1.2	2.523±0.008	4.9±0.7	6.6±9.9
3×10^{13}	6.5±1.0	2.535±0.009	4.6±0.7	22.1±10.8
6×10^{13}	6.0±0.6	2.533±0.006	5.4±0.5	10.7±7.9
1×10^{14}	5.4±0.6	2.533±0.006	6.0±0.6	13.7±8.9
2×10^{14}	3.5±0.6	2.537±0.014	5.7±1.3	12.2±18.8
3×10^{14}	3.1±0.7	2.535±0.014	5.2±1.3	7.7±18.2
1×10^{15}	Nanoparticles dissolved in the matrix as inferred from XTEM results.			

TABLE III. Cu-Cu bonding fraction was determined by XANES analysis. Note that an error of 5% was taken as a reasonable estimate (Ref. 40) The last column is the Cu-Cu coordination number around Cu within the remainder of the nanoparticle material.

Sample	Measured Cu-Cu coordination number (atoms)	Cu-Cu fraction (%)	Real Cu-Cu coordination number (atoms)
Unirr. nanoparticles	10.1±1.1	100±5	10.1±1.2
1×10^{13}	8.5±1.2	100±5	8.5±1.3
3×10^{13}	6.5±1.0	90±5	7.2±1.2
6×10^{13}	6.0±0.6	70±5	8.6±1.1
1×10^{14}	5.4±0.6	60±5	9.0±1.2
2×10^{14}	3.5±0.6	40±5	8.8±2.3
3×10^{14}	3.1±0.7	25±5	12.4±3.7
1×10^{15}		0±5	
3×10^{15}		0±5	
1×10^{16}		≡0	

copy as a function of irradiation fluence. Measurements were performed at beamline 20-B of the Photon Factory, Japan, at the Cu *K*-edge (8.979 keV) at 12 K to minimize thermal disorder. Fluorescence spectra were recorded with a multielement solid state Ge detector and the Si (111) monochromator was detuned by 50% for harmonic rejection. EXAFS samples of Cu nanoparticles were prepared in two steps and were also used for SAXS measurements. First, the Si substrate below the SiO_2 film was removed using a combination of mechanical grinding and selective chemical etching (KOH in H_2O). Second, the 2 μm SiO_2 films were stacked together (to an effective Cu thickness comparable to that of the bulk standard) and embedded in an EXAFS cell sealed by x-ray transparent Kapton film. In general, the resulting increase in the effective amount of absorbing element (Cu) and elimination of scattering from the substrate (Si) significantly improved the signal-to-noise ratio.[24] Fluorescence spectra were recorded to a photoelectron wave number (k) maximum of 18 $Å^{-1}$ for both nanoparticle and bulk samples. The effective Cu concentration of all samples was sufficiently low to inhibit self-absorption. The Cu *K*-edge fluorescence signal comprised 50–70 % of the incoming count rate, the latter maintained within the linear counting regime of the detector.

EXAFS data processing and analysis were performed following standard methods.[29] The EXAFS oscillations were isolated from the raw absorption by background subtraction and subsequent splining utilizing the Athena software.[30] The normalized EXAFS was then k^3 weighted and Fourier transformed (FT) over a k range of 3.0–16.3 $Å^{-1}$. The first nearest neighbor coordination shell was isolated by inverse transforming over a non-phase-corrected radial distance range of 1.74–2.74 Å. Structural parameters were determined for the first nearest neighbor shell by nonlinear least squares fitting using IFEFFIT,[31] with phases and backscattering amplitudes calculated *ab initio* with the FEFF8.1[32] code. The amplitude reduction factor (S_0^2) and threshold energy (E_0) were determined from the unirradiated bulk standard and held constant for the analysis of all other samples. The coordination number, bondlength, Debye-Waller factor and third cumulant[33] were determined. The latter is the asymmetric deviation from a Gaussian bondlength distribution. The reported errors are the fitting errors, comparing the simulated spectra with the transformed raw EXAFS, as recommended by the International XAFS Society.[34]

III. RESULTS AND DISCUSSION

In Secs. III A–III C we will present and discuss results of the ion irradiation of embedded Cu nanoparticles (and bulk Cu standard) in terms of shape and size (Sec. III A), short-range atomic structure and intermixing (Sec. III B), and recrystallization (Sec. III C). In particular, we will argue for the existence of an amorphous Cu phase present in the nanoparticles after ion irradiation with a fluence of 1×10^{14} ions/cm^2 (hereafter units will be omitted for simplicity) and in Sec. III C we also suggest a mechanism for the amorphization.

A. Nanoparticle shape and size

Figure 1 shows a range of XTEM micrographs, including (a) unirradiated and (b)–(e) irradiated nanoparticles (successive irradiation fluences of 6×10^{13}, 1×10^{14}, 3×10^{14}, and 1×10^{15}). The nanoparticles are of spherical shape both before and after irradiation (apart from the highest fluence). Prior to irradiation, the nanoparticles exhibit the fcc structure, as measured by electron diffraction (not shown) and are randomly oriented within the amorphous SiO_2. In the inset of Fig. 1(a), the (111) lattice planes of fcc Cu are discernible in the high-resolution image. Upon irradiation at 1×10^{14}, lattice fringes could not be resolved.

For the unirradiated nanoparticles, the average volume-weighted diameter determined by XTEM was ~29 Å with a full width at half maximum (FWHM) of ~15 Å. With reference to Fig. 1, upon irradiation (at fluences of 6×10^{13} and 1×10^{14}) the nanoparticle size distribution does not change appreciably. Further irradiation (3×10^{14}) causes an apparent decrease in nanoparticle density as well as average size.[35] After irradiation at 1×10^{15}, no nanoparticles are observable although the presence of Cu was confirmed by energy dis-

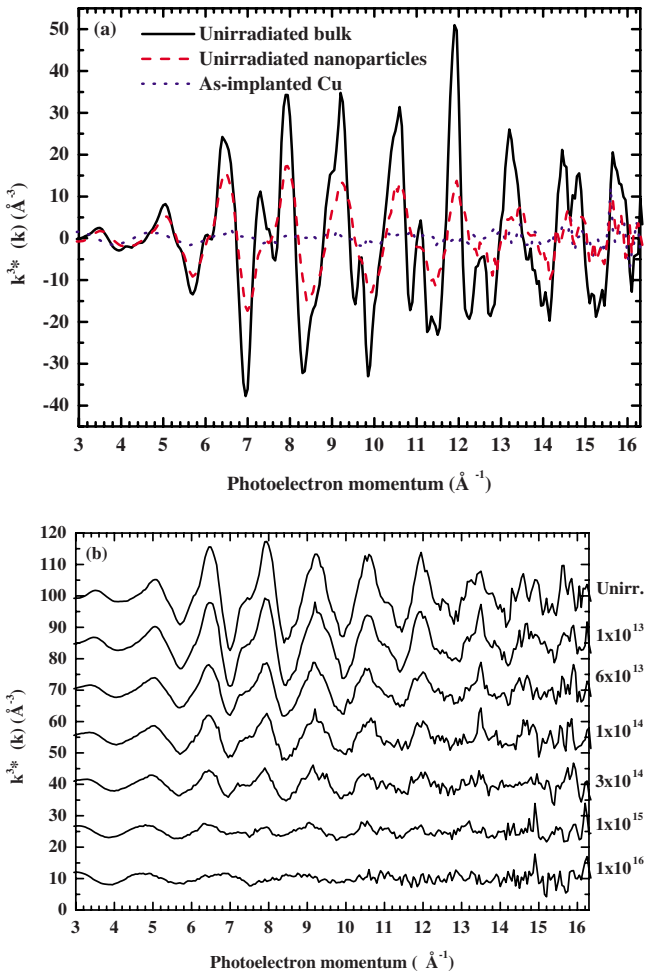

FIG. 3. (Color online) k^3-weighted EXAFS spectra for (a) the unirradiated bulk standard, as-implanted Cu and unirradiated nanoparticle sample and (b) the nanoparticle sample as a function of ion irradiation fluence.

persive x-ray analysis. We infer that a fluence of 1×10^{15} causes sufficient ion beam mixing to dissolve the nanocrystals in the matrix.

Figure 2(a) shows the measured SAXS profile (symbols) and corresponding fitted data (solid lines) for both unirradiated and irradiated nanoparticles. Minor changes in the SAXS profile are observed for irradiated nanoparticles up to a fluence of 3×10^{14}. For fluences 1×10^{15} or greater the SAXS profile is similar to that of the as-implanted sample (not shown), consistent with the dissolution of the nanoparticles observed by XTEM. Figure 2(b) shows the volume-weighted size distributions obtained by SAXS as a function of fluence. For the unirradiated sample, the distribution obtained from XTEM is also included (columns). We note that SAXS yields a smaller average diameter (~25 Å) than XTEM measurements (~29 Å) consistent with the difficulty in resolving the smaller nanoparticles in the microscope. Table I summarizes the size distribution obtained from SAXS for irradiation fluences up to 3×10^{14}. A general increase in average volume-weighted diameter is observed with increasing irradiation fluence up to 2×10^{14}, indicating softening of the nanoparticle/matrix interface. At fluences where irradiation yields nanoparticle dissolution ($\geq1\times10^{15}$) SAXS is insensitive to Cu atoms dissolved in the matrix.

In summary, the nanoparticles were spherical (XTEM) and of the fcc structure (electron diffraction) prior to ion irradiation. Following ion irradiation, the nanoparticles retained their spherical shape (XTEM) while the average nanoparticle diameter increased (SAXS) up to a fluence of 2×10^{14}. Residual crystallinity was not apparent (electron diffraction) after ion irradiation to a fluence of 1×10^{14}. Fluences greater than 3×10^{14} yielded nanoparticle dissolution (XTEM) into the matrix.

B. Short-range atomic structure and intermixing

Figure 3(a) displays k^3-weighted EXAFS spectra for the as-implanted, unirradiated and bulk samples over the fitted k range of 3.0–16.3 $Å^{-1}$. The much reduced amplitudes for the as-implanted sample are consistent with the absence of nanoparticles. Upon annealing, the nanoparticle and bulk sample spectra are similar in shape though differ in magnitude due to the formation of Cu nanoparticles with fcc structure as discussed below. Figure 3(b) displays k^3-weighted EXAFS spectra for the nanoparticle samples as a function of ion irradiation fluence. Note the decrease in EXAFS amplitude with increasing fluence. For fluences of 1×10^{15} and above, the spectra are comparable to that of the as-implanted sample [cf. Fig. 3(a)] consistent with dissolution of the nanoparticles.

Figures 4(a) and 4(b) show the FTs corresponding to spectra in Figs. 3(a) and 3(b). As expected, the spectrum of the unirradiated nanoparticle sample is comparable, though of lesser magnitude, to that of the bulk fcc sample. The first four pronounced peaks correspond to the first four nearest neighbor shells surrounding a Cu atom (at $r=\sim2.5$, 3.6, 4.3, and 5.0 Å, respectively). The reduced amplitude is indicative of a reduced coordination number and/or increased Debye-Waller factor for the Cu nanoparticles. Both are a consequence of the increased surface-to-bulk ratio and the relaxation/reconstruction of undercoordinated surface atoms. Upon irradiation we observe a decrease in peak height and concurrent increase in FWHM of the first nearest neighbor, consistent with a further decrease in average coordination number and/or increase in Debye-Waller factor. This result is consistent with a disordered phase, ion beam mixing and/or a decrease in nanoparticle size. We will argue below that a combination of these scenarios is present at a fluence of 1×10^{14}.

For an irradiation fluence of 1×10^{14}, the first nearest neighbor is still apparent, while the structure at higher r is much diminished. Eventually (at a fluence of $\sim1\times10^{16}$) all four nearest neighbors disappear and the spectrum is similar to that of the as-implanted sample. For irradiation fluences $\geq1\times10^{15}$, a peak between the Cu absorber and first nearest neighbor Cu scatterers appears at ~1.8 Å consistent with Cu-O bonding.[24] The dissolution of Cu in the matrix (XTEM) yields an increase in Cu-O bonding at the expense of Cu-Cu bonding. The inset in Fig. 4(b) shows the FTs of the unirradiated bulk standard compared to a selection of

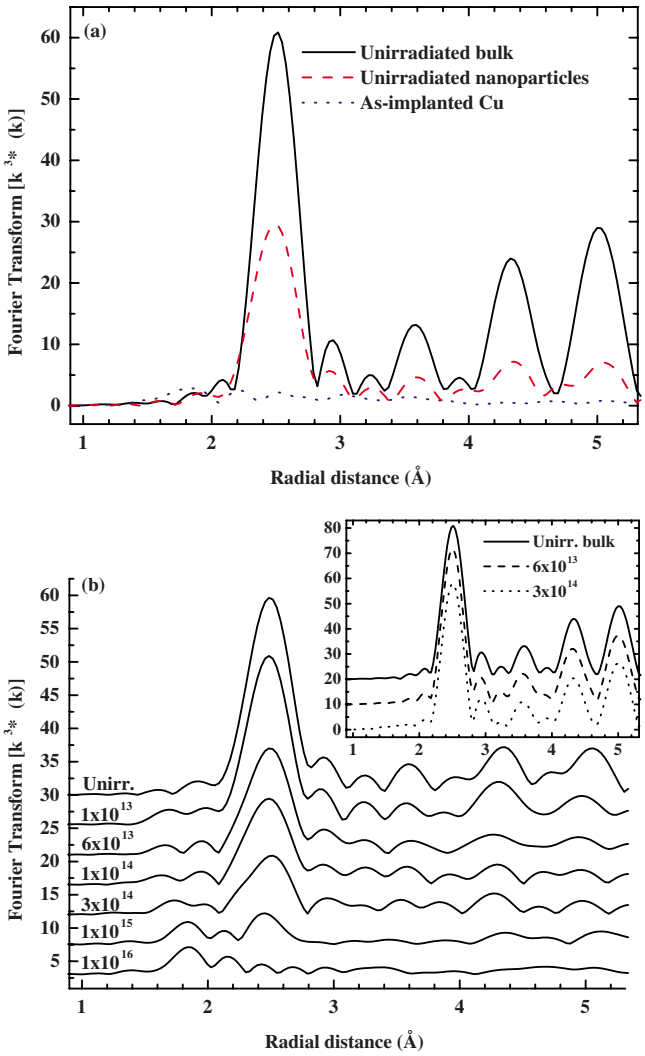

FIG. 4. (Color online) Fourier-transformed EXAFS spectra for (a) the unirradiated bulk standard, as-implanted Cu and unirradiated nanoparticle sample, and (b) the nanoparticle sample as a function of ion irradiation fluence (offset) with (inset) the bulk standard for selected ion irradiation fluences.

irradiated standards. Clearly, structural changes occurring in the bulk upon irradiation are negligible, consistent with the inability to amorphize a bulk elemental metal with ion irradiation.[12]

The average coordination number, bondlength, Debye-Waller factor, and the third cumulant for the first nearest neighbor are listed in Table II and presented in Figs. 5(a)–5(d). We note the significantly higher structural disorder (Debye-Waller factor) for the Cu nanoparticles pre-irradiation as compared to the bulk, indicating the influence of the surface atoms (approximately half the atoms are located at the surface). In general, the bulk Cu is not affected by ion irradiation [up to a fluence equivalent to ~50 displacements per atom (dpa)] while the Cu nanoparticles exhibit a decrease in coordination number and concurrent increase in bondlength, Debye-Waller factor and third cumulant. In particular, the bondlength and Debye-Waller factor increase by ~0.5 and 24%, respectively, for an ion irradiation fluence of 1×10^{14} equivalent to ~0.16 dpa. Previously we reported similar results for ion irradiated Ge nanoparticles,[14] which were rendered amorphous at ~0.01 dpa with an increase in the Debye-Waller factor by ~25% (the bulk standard was rendered amorphous by irradiation equivalent to ~1 dpa). Furthermore, a positive third cumulant signifies a non-Gaussian bondlength distribution skewed towards longer bondlengths again consistent with an amorphous phase[36] as previously reported for amorphous Fe.[9] The large decrease in coordination number can be attributed to several factors as discussed below.

Figure 6 shows dynamic ion irradiation simulations (TRIDYN[37]) for a 25 Å thick Cu film embedded at a depth of 0.6 μm within a SiO_2 matrix to estimate the degree of intermixing upon irradiation by 5.0 MeV Sn ions. For visual simplicity the abscissa has its origin at the center of the Cu film. Fluences of (1×10^{14})–(1×10^{15}) are shown and in the former only a slight decrease (~2%) in the peak Cu concentration is observed.[38] While the FWHM does not increase, the interface is no longer a step function consistent with intermixing and less-well-defined nanoparticle/matrix interfaces. On the other hand, at a fluence of 1×10^{15} we observe significant intermixing, e.g., the peak Cu concentration is reduced by ~50% and the FWHM is nearly doubled. Similarly, an equally significant increase in both O and Si concentration is observed within the Cu film (not shown). This result is consistent with the ion-irradiation-induced dissolution of nanoparticles as presented above.

The presence of both Cu-Cu and Cu-O environments must be considered when interpreting the trends for the short-range atomic structure as determined by EXAFS. The ion-irradiation-induced production of Cu-O bonds will reduce the apparent average Cu-Cu coordination number of the Cu nanoparticles. [Note that Cu-O bonds will not affect the measured Cu-Cu bondlength, Debye-Waller factor or third cumulant as presented in Figs. 5(b)–5(d).] For the unirradiated sample, we can apply the following approximation relating the average Cu-Cu coordination number (Π_{av}) and diameter (D) for a spherical 12-fold coordinated nanoparticle[39]:

$$\Pi_{av} = 12[1 - (3/2D)R], \tag{1}$$

where R is the bulk bond length. Using the average diameter measured by SAXS and the bulk bondlength measured by EXAFS, we calculate an average Cu-Cu coordination number of ~10.1 atoms in excellent agreement with the measured value. Correlating such results with XANES described below, we conclude that prior to irradiation all implanted Cu is incorporated in the nanoparticles (i.e., not dissolved in the matrix).

To determine the fraction of Cu atoms in oxide (Cu-O bonds) and metal (Cu-Cu bonds) environments after irradiation, analysis of the x-ray absorption near-edge structure (XANES) was undertaken. Figure 7 shows XANES spectra for the irradiated nanoparticles compared to that of the unirradiated nanoparticles and bulk crystalline samples. The difference in the latter two is attributed to finite size effects. After irradiation with a fluence of 1×10^{16} the XANES is consistent with Cu dispersed in SiO_2,[40] exhibiting a charac-

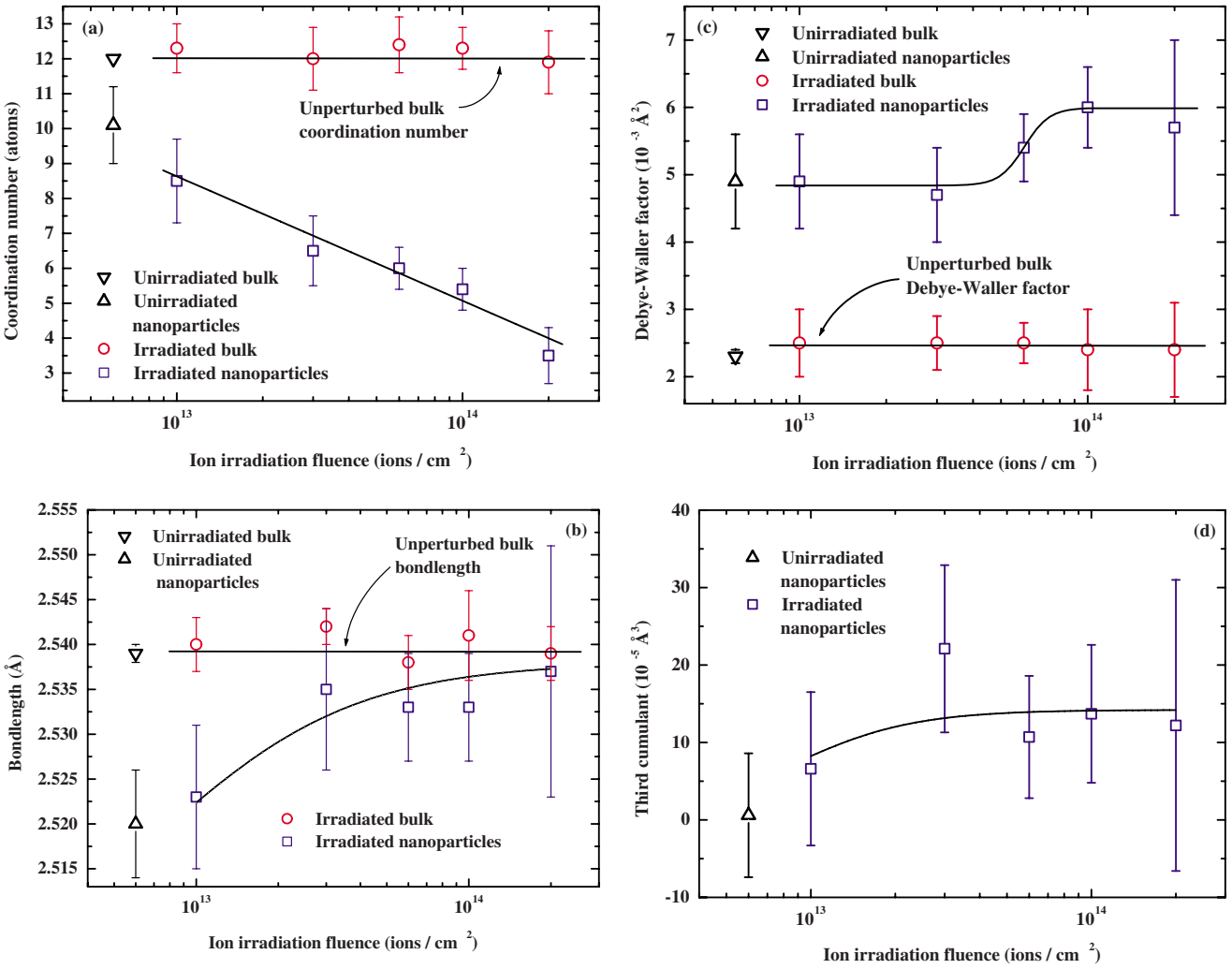

FIG. 5. (Color online) Ion irradiation fluence dependence of the four structural parameters of the first nearest neighbor shell of bulk and nanoparticle samples: (a) Coordination number, (b) bondlength, (c) Debye-Waller factor, and (d) third cumulant.

teristic pre-edge feature typical of Cu_2O.[24] We estimated the fraction of dispersed Cu by fitting the spectrum of each irradiated nanoparticle sample in the energy range 8.95–9.10 keV to a linear combination of the unirradiated and 1×10^{16} spectrum. Examples of these fits are shown in Fig. 8(a). Clearly, the irradiated samples contain Cu atoms in two distinct phases, i.e., Cu oxides and/or nanoparticles. Table III lists the results, which are also presented graphically in Fig. 8(b). Shown is the fraction of Cu bound to Cu in the form of nanoparticles as a function of ion irradiation fluence. As expected, we observe a decrease in Cu-Cu fraction, or equivalently an increase in the Cu-O fraction, with increasing fluence. At 1×10^{14} the fraction of dispersed Cu is ~40%. Also displayed in Fig. 8(b) is the evolution of the coordination number, as a function of irradiation fluence, after the Cu-O fraction has been taken into account. We observe that the latter saturates at ~9 atoms at 1×10^{14} (at 3×10^{14} the influence of Cu-O EXAFS signal causes the measurement errors to increase significantly).

SRIM simulations show that the recoil energies of matrix and Cu atoms are sufficient to displace any of the constituent atoms ~3 Å (approximately 1–2 bondlengths),[25] consistent

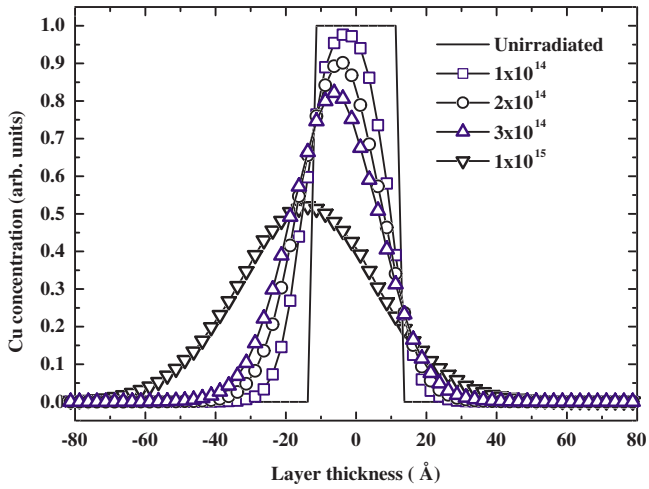

FIG. 6. (Color online) Dynamic TRIM (TRIDYN [37]) simulations of ion beam mixing in 25 Å Cu embedded in SiO_2 induced by 5.0 MeV Sn^{3+} irradiation. Note that the abscissa has its origin at the center of the Cu film and that the irradiated spectra are shifted due to sputtering at the surface.

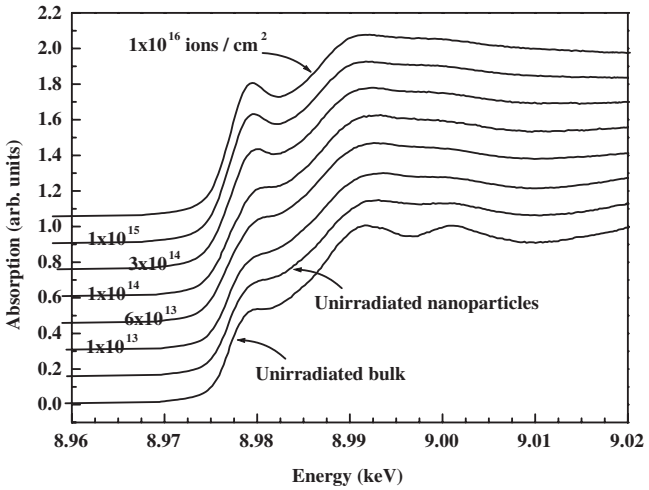

FIG. 7. XANES spectra of the unirradiated bulk standard and nanoparticle samples as a function of ion irradiation fluence.

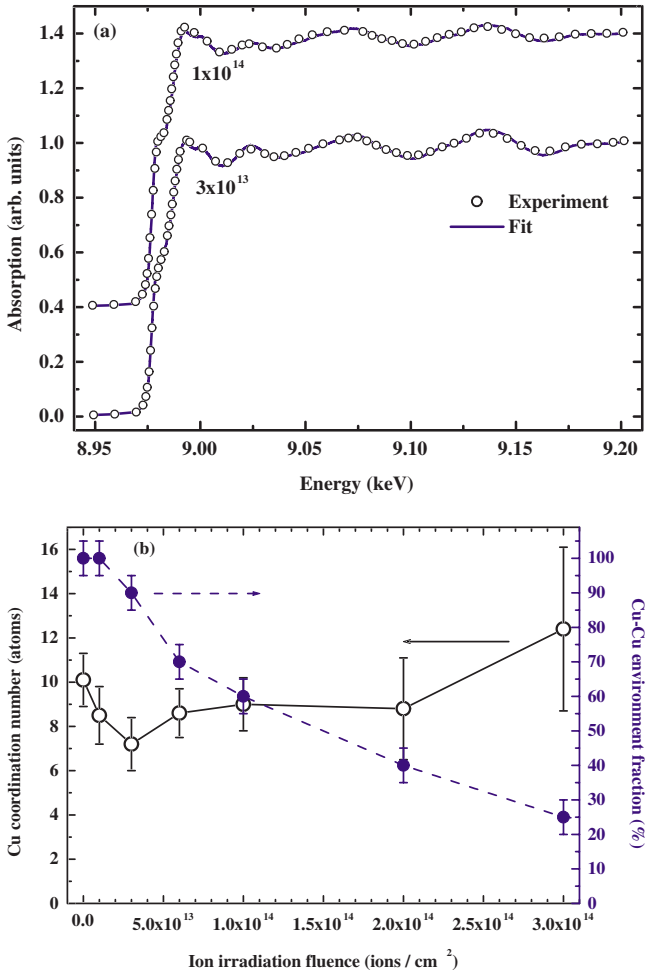

FIG. 8. (Color online) (a) Irradiated Cu nanoparticle XANES spectra fitted with a linear combination of the unirradiated and 1×10^{16} spectrum. (b) Cu-Cu fraction and coordination number (adjusting for the former) as a function of ion irradiation fluence.

with TRIDYN results and the less-well-defined nanoparticle/matrix interfaces. Additionally, the highly nonequilibrium nature of ion irradiation causes strong Si-O bonds to break.[35] Cu atoms recoil into the matrix will, under the minimum diffusion conditions present (LNT), preferentially bond with O rather than Cu (cf. bond enthalpies for Cu-O and Cu-Cu[41]). The net effect of ion irradiation, viewed simplistically, but in agreement with XANES presented above, is a reduction in diameter of the elemental Cu nanoparticles (cores) surrounded by an environment rich in Cu-O bonds.[42] For the latter, the Cu oxidation state and local coordination is similar to that in Cu_2O, albeit not in a crystalline form, as determined by XANES analysis above.[24] At a fluence of 1×10^{14}, the metallic core has an average coordination number of 9.0 ± 1.2 atoms. We stress that the presence of Cu-O bonds do not contribute to the (average) Cu-Cu bondlength, Debye-Waller factor, or third cumulant.

A crystalline Cu_2O standard (diluted powder) was also measured in EXAFS fluorescence mode. The first nearest neighbor consisting of two O atoms was analyzed and compared to that for the as-implanted and 1×10^{16} sample. A k^1 weighting was applied and the first O coordination shell was then isolated by inverse transforming over a non-phase-corrected r range of 0.6–2.0 Å. The results are summarized in Table IV (S_0^2 and E_0 values were determined from the standard and kept constant thereafter). From XTEM and XANES presented above, we know that a fluence of 1×10^{16} leads to complete dissolution of the nanoparticles. From the EXAFS results presented in Table IV we note that, as expected, both prior to the formation of nanoparticles and after dissolution of the nanoparticles there is predominantly Cu-O bonding. The local coordination and oxidation state is comparable to that of the Cu_2O standard.

The influence of ion irradiation on the short-range atomic structure is best illustrated by the radial distribution function (RDF). The RDFs were reconstructed from the first three cumulants[43] of the Cu-Cu interatomic distance distribution following the method of Dalba and Fornasini[44] and using a photoelectron mean free path of 8 Å. Figure 9 shows the reconstructed RDFs for the nanoparticles prior to and after ion irradiation (1×10^{14}) using the corrected Cu-Cu coordination number of 9.0 for the latter, while the bondlength, Debye-Waller factor and third cumulant are those listed in Table II. The RDF of the unirradiated bulk is included as a reference and all RDFs are normalized to the number of nearest neighbors. Upon irradiation of the nanoparticles we observe the following: (1) A decreased Cu-Cu coordination

TABLE IV. Cu-O EXAFS analysis: Structural parameters for the first nearest O neighbor in a Cu_2O standard, the as-implanted sample, and the 1×10^{16} sample. Since O is a low-Z scatterer, k^1 weighting was applied to emphasize the Cu-O bonds.

Sample	Coordination number (atoms)	Bondlength (Å)	Debye-Waller factor ($\times10^{-3}$ Å^2)
Cu_2O standard	2 (fixed)	1.82±0.02	4.3±2.6
As-implanted	1.9±0.2	1.84±0.01	6.3±2.3
1×10^{16}	2.0±0.3	1.84±0.01	7.2±2.8

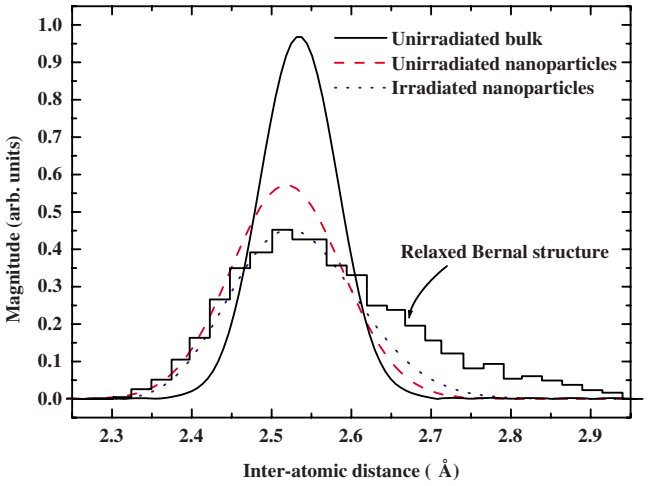

FIG. 9. (Color online) Reconstructed radial distribution functions (RDFs) of the first nearest neighbor shell of unirradiated and irradiated (1×10^{14} ions/cm^2) nanoparticles compared to the RDFs of the unirradiated bulk standard and a theoretical prediction from a dense random packing of equal spheres model (relaxed Bernal structure[36]).

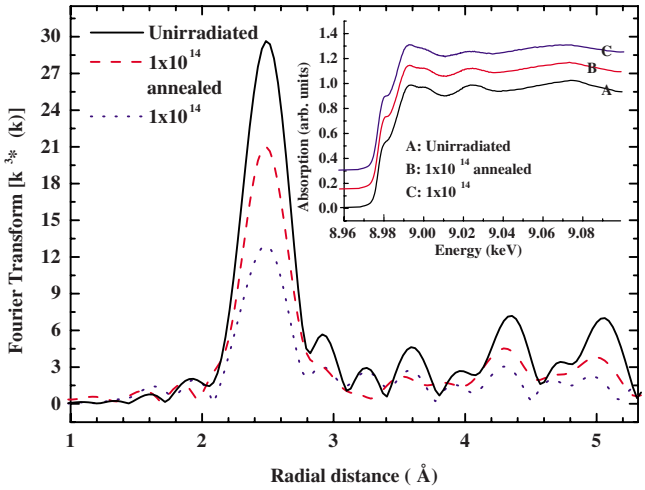

FIG. 10. (Color online) Fourier-transformed EXAFS spectra for the nanoparticle sample prior to irradiation, after irradiation at a fluence of 1×10^{14}/cm^2 and after subsequent reannealing at 350 °C. The inset shows XANES spectra for the same sample series.

number and increased Debye-Waller factor consistent with an amorphous phase *and* reduced size and (2) an increased bondlength and positive third cumulant consistent with an amorphous phase but *not* with a reduced size.[24] We thus suggest the spectrum of the irradiated Cu nanoparticles represents the amorphous phase structure. For comparison, a theoretical prediction from a dense random packing model for an elemental amorphous bulk metal is included (relaxed Bernal structure[36]). The experimental and theoretical RDFs for the amorphous phase are consistent and the marked asymmetry in both spectra is readily apparent.

Even in the absence of ion irradiation, the minimum-energy crystallographic phase of Cu nanoparticles need not be fcc. Indeed, Reinhard *et al.* reported that *non*-embedded Cu nanoparticles (2.0–2.5 nm diameter) prefer an icosahedral structure consistent with theoretical predictions.[45] The first nearest neighbor shell of the icosahedral structure is split into two shells at r_1 and r_2 where r_2 is ~5% greater than r_1.[46] Our EXAFS measurements, as presented above, are *not* consistent with such structure. The surrounding matrix may inhibit formation of the icosahedral structure.

In summary, though the unirradiated Cu nanoparticles and bulk standard have a common fcc structure, the former exhibits significantly higher static disorder relative to the latter. While ion irradiation induces negligible changes in the bulk standard, the structural parameters of the nanoparticles are perturbed significantly. The decrease in Cu-Cu coordination number and increase in bondlength, Debye-Waller factor and third cumulant are all consistent with an amorphous phase. The corresponding RDF is markedly asymmetric and skewed towards longer bondlengths, consistent with a dense random packing model.[36] Under the appropriate conditions, ion irradiation thus yields disordering, then amorphization and dissolution of Cu nanoparticles.

C. Recrystallization and a proposed mechanism for amorphization

The sample irradiated to a fluence of 1×10^{14} was annealed at 350 °C for 1 h in forming gas. Figure 10 shows the Fourier-transformed EXAFS spectra for the sample prior to irradiation, after irradiation and after annealing. XANES measurements for the same sample series are shown in the inset. Analysis of the latter showed a virtually unchanged Cu-Cu fraction of ~60% upon annealing (58±5%). The amplitude of the annealed sample increases relative to the irradiated sample due to an increase in Cu-Cu coordination number and decrease in Debye-Waller factor. The amplitude of the annealed sample remains less than the unirradiated sample due to the continued presence of the Cu-O fraction. Table V lists the structural parameters for these samples. In

TABLE V. Structural parameters of Cu nanoparticles prior to irradiation, after irradiation at a fluence of 1×10^{14}/cm^2 and after subsequent reannealing at 350 °C extracted by first nearest neighbor EXAFS analysis (k^3 weighted).

Sample	Cu-Cu coordination number (atoms)	Bondlength (Å)	Debye-Waller factor ($\times10^{-3}$ Å^2)	Third cumulant ($\times10^{-5}$ Å^3)
Unirr. nanoparticles	10.1±1.2	2.520±0.006	4.9±0.7	0.6±8.0
1×10^{14}	9.0±1.2	2.533±0.006	6.0±0.6	13.7±8.9
Reannealed	10.3±1.2	2.522±0.005	4.9±0.6	1.9±8.5

summary, we observe that the structural parameters of the recrystallized and unirradiated samples are near identical, which demonstrates that (1) the amorphous phase has been recrystallized and (2) the parameters listed for the amorphous phase did not result from the presence of recoiled lattice atoms.

The Cu nanoparticles investigated in the present report were clearly perturbed, relative to the bulk standard, prior to irradiation. Though the fcc structure was retained, the inherent structural disorder (Debye-Waller factor) of the Cu nanoparticles was twice that of the bulk phase. The latter is the result of bonding distortions at the nanoparticle/matrix interface[47] and the concomitant increase in the nanoparticle structural energy. Given that approximately half the atoms reside at the interface, the influence of these bonding distortions is necessarily great, in marked contrast to the bulk standard. (This is also in contrast to the irradiation of ~ 8 nm diameter Cu nanoparticles where $<15\%$ of the atoms reside at the surface for which an amorphous component was not observed[48]). The high surface-to-bulk ratio of the nanoparticles can account not only for the initially large Debye-Waller factor, but may also serve as a preferential site for the nucleation of the amorphous phase upon ion irradiation and/or stabilize such a phase subsequent to formation.

IV. CONCLUSIONS

In conclusion, we have investigated the atomic structure of ion irradiated Cu nanoparticles synthesized in SiO_2 by ion implantation and thermal annealing. Prior to irradiation, all Cu was in the form of nanoparticles exhibiting the fcc structure though the inherent structural disorder was twice that of the bulk. Upon irradiation the long-range order vanished while the fraction of dissolved Cu atoms increased due to collisional mixing. The amount of oxide increased until the nanoparticles were completely dispersed in the matrix at fluences $\geq 1\times 10^{15}$ ions/cm^2. At an intermediate fluence of 1×10^{14} ions/cm^2, the Debye-Waller factor of the first nearest neighbor shell increased by $\sim 25\%$. Simultaneously, the bondlength and third cumulant increased while the Cu-Cu coordination number decreased. Such observations are consistent with the dense random packing model proposed for amorphous elemental metals. Moreover, after the amorphized sample was annealed at 350 °C for 1 h, the initial pre-irradiation structure was recovered.

ACKNOWLEDGMENTS

B.J., P.K., G.J.F., D.J.C., and M.C.R. were supported by the Australian Synchrotron Research Program, funded by the Commonwealth of Australia. P.K. and M.C.R. thank the Australian Research Council for financial support. Use of the Advanced Photon Source was supported by the U.S. Department of Energy, Office of Science, Office of Basic Energy Sciences, under Contract No. DE-AC02-06CH11357.

*Corresponding author. Present address: Australian Nuclear Science and Technology Organisation, Menai NSW 2234, Australia. FAX: +81 298 64 7959. bej@anbf2.kek.jp

[1] W. Klement, R. H. Willens, and P. Duwez, Nature (London) **187**, 869 (1960).
[2] T. R. Anatharaman, *Metallic Glasses* (Trans. Tech., Aedermannsdorf, Switzerland, 1984).
[3] P. Haasen and R. I. Jaffee, *Amorphous Metals and Semiconductors* (Pergamon, London, 1986).
[4] *Rapidly Quenched Metals*, edited by H. Steeb and H. Warlimont (Eds.), (Elsevier, Amsterdam, 1985).
[5] A. S. Clarke and J. D. Wiley, Phys. Rev. B **35**, 7350 (1987).
[6] L. Fejes Toth, *Regular Figures* (Pergamon, New York, 1964), pp. 292–300.
[7] J. R. Cahoon, Can. J. Phys. **82**, 291 (2004).
[8] See, e.g., D. B. Miracle, Nat. Mater. **3**, 697 (2004).
[9] G. J. Long, D. Hautot, Q. A. Pankhurst, D. Vandormael, F. Grandjean, J. P. Gaspard, V. Briois, T. Hyeon, and K. S. Suslick, Phys. Rev. B **57**, 10716 (1998).
[10] Y. Koltypin, G. Katabi, X. Cao, R. Prozorov, and A. Gedanken, J. Non-Cryst. Solids **201**, 159 (1996).
[11] R. V. Kumar, Y. Mastai, Y. Diamant, and A. Gedanken, J. Mater. Chem. **11**, 1209 (2001).
[12] K. Nordlund, M. Ghaly, R. S. Averback, M. Caturla, T. Diaz de la Rubia, and J. Tarus, Phys. Rev. B **57**, 7556 (1998).
[13] We note, however, that amorphization by ion irradiation is achievable when the implanted ion is a chemically-active impurity and is present at sufficiently high concentrations; see, e.g., A. Benyagoub and L. Thomé, Phys. Rev. B **38**, 10205 (1988) and references therein.
[14] M. C. Ridgway, G. de M. Azevedo, R. G. Elliman, C. J. Glover, D. J. Llewellyn, R. Miller, W. Wesch, G. J. Foran, J. Hansen, and A. Nylandsted-Larsen, Phys. Rev. B **71**, 094107 (2005).
[15] C. M. Johnson, T. D. Thompson, M. C. Ridgway, and V. Gurarie, Nucl. Instrum. Methods Phys. Res. B, **141**, 629 (1998).
[16] M. L. Brongersma, E. Snoeks, T. van Dillen, and A. Polman, J. Appl. Phys. **88**, 59 (2000).
[17] A. H. Sørensen, E. Johnson, K. K. Bourdelle, A. Johansen, H. H. Andersen, and L. Sarholt-Kristensen, Philos. Mag. A **75**, 1533 (1997).
[18] C. J. Rossouw and S. E. Donnelly, Phys. Rev. Lett. **55**, 2960 (1985).
[19] Q. Xu, I. D. Sharp, C. W. Yuan, D. O. Yi, C. Y. Liao, A. M. Glaeser, A. M. Minor, J. W. Beeman, M. C. Ridgway, P. Kluth, J. W. Ager III, D. C. Chrzan, and E. E. Haller, Phys. Rev. Lett. **97**, 155701 (2006).
[20] Y. Takeda, J. P. Zhao, C. G. Lee, V. T. Gritsyna, and N. Kishimoto, Nucl. Instrum. Methods Phys. Res. B **166-167**, 877 (2000).
[21] N. Kishimoto, N. Okubo, O. A. Plaksin, N. Umeda, J. Lu, and Y. Takeda, Nucl. Instrum. Methods Phys. Res. B **218**, 416 (2004).
[22] G. Kuri, Appl. Phys. A: Mater. Sci. Process. **68**, 699 (1999).
[23] B. Johannessen, P. Kluth, D. J. Llewellyn, G. J. Foran, D. J. Cookson, and M. C. Ridgway, Appl. Phys. Lett. **90**, 073119

(2007).
[24] B. Johannessen, P. Kluth, C. J. Glover, G. de M. Azevedo, D. J. Llewellyn, G. J. Foran, and M. C. Ridgway, J. Appl. Phys. **98**, 024307 (2005).
[25] J. F. Ziegler, J. P. Biersack, and U. Littmark, *The Stopping and Range of Ions in Matter* (Pergamon Press, New York, 1985).
[26] A. Gunier and G. Fournet, *Small-Angle Scattering of X-rays* (Wiley, New York, 1955).
[27] C. S. Tsao and T. L. Lin, J. Appl. Crystallogr. **30**, 353 (1997).
[28] O. Glatter, J. Appl. Crystallogr. **21**, 886 (1988).
[29] D. E. Sayers and B. A. Bunker, in *X-ray Absorption: Principles, Applications and Techniques of EXAFS, SEXAFS and XANES*, edited by D. C. Koningsberger and R. Prins (Wiley, New York, 1998), p. 211.
[30] B. Ravel and M. Newville, J. Synchrotron Radiat. **12**, 537 (2005).
[31] M. Newville, J. Synchrotron Radiat. **8**, 322 (2001).
[32] J. J. Rehr and R. C. Albers, Rev. Mod. Phys. **72**, 621 (2000).
[33] M. C. Ridgway, C. J. Glover, K. M. Yu, G. J. Foran, C. Clerc, J. L. Hansen, and A. Nylandsted Larsen, Phys. Rev. B **61**, 12586 (2000).
[34] IXS: http://ixs.iit.edu
[35] We note that the nanoparticle density is inherently difficult to measure by XTEM; however, all samples were prepared following the same technique, including the final ion beam milling.
[36] L. v Heimendahl, J. Phys. F: Met. Phys. **5**, L141 (1975).
[37] W. Möller and W. Eckstein, Nucl. Instrum. Methods Phys. Res. B, **2**, 814 (1984).
[38] We note, however, that this simulation underestimates the amount of intermixing due to the three-dimensional nature of the nanoparticles.
[39] S. de Panfilis, F. d'Acapito, V. Haas, H. Konrad, J. Weissmüller, and F. Boscherini, Phys. Lett. A **207**, 397 (1995).
[40] F. d'Acapito, S. Mobilio, G. Battaglin, E. Cattaruzza, F. Gonella, F. Caccavale, P. Mazzoldi, and J. R. Regnard, J. Appl. Phys. **87**, 1819 (2000).
[41] Webelements, URL www.webelements.com
[42] The diameter estimated by SAXS measurements is the diameter including the surface Cu-O layer, assuming the latter is sufficiently packed to have a charge density comparable to that of the Cu core, while comparably different from that of the surrounding SiO_2 matrix.
[43] The first three cumulants correspond to the bondlength, Debye-Waller factor, and the asymmetric deviation from a Gaussian distribution.
[44] G. Dalba and P. Fornasini, J. Synchrotron Radiat. **4**, 243 (1997).
[45] D. Reinhard, B. D. Hall, P. Berthoud, S. Valkealahti, and R. Monot, Phys. Rev. Lett. **79**, 1459 (1997).
[46] J. Oviedo and R. E. Palmer, J. Chem. Phys., **117**, 9548 (2002).
[47] P. Kluth, B. Johannessen, V. Giraud, A. Cheung, C. J. Glover, G. de M. Azevedo, G. J. Foran, and M. C. Ridgway, Appl. Phys. Lett. **85**, 3561 (2004).
[48] B. Johannessen, P. Kluth, C. J. Glover, S. M. Kluth, G. J. Foran, D. J. Cookson, D. J. Llewellyn, and M. C. Ridgway, Nucl. Instrum. Methods Phys. Res. B **250**, 210 (2006).